# Magnetohydrodynamically generated velocities in confined plasma

Jorge A. Morales, Wouter J. T. Bos, Kai Schneider, and David C. Montgomery

Citation: Physics of Plasmas (1994-present) **22**, 042515 (2015); doi: 10.1063/1.4918774
View online: http://dx.doi.org/10.1063/1.4918774
View Table of Contents: http://scitation.aip.org/content/aip/journal/pop/22/4?ver=pdfcov
Published by the AIP Publishing



# Magnetohydrodynamically generated velocities in confined plasma

Jorge A. Morales,[1,a)] Wouter J. T. Bos,[1] Kai Schneider,[2] and David C. Montgomery[3]
[1]*LMFA, CNRS, École Centrale de Lyon, Écully, France*
[2]*M2P2, CMI, CNRS, Aix-Marseille Université, Marseille, France*
[3]*Department of Physics and Astronomy, Dartmouth College, Hanover, New Hampshire 03755, USA*

(Received 4 December 2014; accepted 3 April 2015; published online 27 April 2015)

We investigate by numerical simulation the rotational flows in a toroid confining a conducting magnetofluid in which a current is driven by the application of externally supported electric and magnetic fields. The computation involves no microscopic instabilities and is purely magnetohydrodynamic (MHD). We show how the properties and intensity of the rotations are regulated by dimensionless numbers (Lundquist and viscous Lundquist) that contain the resistivity and viscosity of the magnetofluid. At the magnetohydrodynamic level (uniform mass density and incompressible magnetofluids), rotational flows appear in toroidal, driven MHD. The evolution of these flows with the transport coefficients, geometry, and safety factor are described. © *2015 AIP Publishing LLC*. [http://dx.doi.org/10.1063/1.4918774]

## I. INTRODUCTION

Toroidal magnetic plasma confinement has been under investigation since the 1940s when it was recognized as a promising geometry for controlled thermonuclear fusion. Despite all the attention devoted to the idea, there are aspects of it that must be regarded as incomplete, even in theory. The difficulties in many cases reduce to the fact that there is no mathematical description of a magnetically active, dissipative plasma that is tractable, by use of even the fastest supercomputers. Time dependent electromagnetic fields combined with the particle kinetics of plasmas having the range of mass ratios represented among the various charges is simply a too large system to be susceptible to a complete treatment. Enormous simplifying assumptions have to be made to achieve any analytical/numerical progress. A common assumption has been that of an unstable ideal equilibrium whose numerous linear instabilities may reveal insight into the nonlinear dynamical behavior that is observed. It must be conceded that any description that is manageable at a detailed level will omit certain important features of a real plasma in a tokamak or reversed field pinch (RFP), and at this stage it is to some extent a matter of taste as to which incomplete theoretical description is adopted for study.

In the following pages, we report the investigation of one such description: a voltage driven, dissipative magnetohydrodynamic (MHD) fluid with non-ideal toroidal boundary conditions for the velocity field. We omit some features that would be desirable and which seem reasonable to inject, at a later date, one at a time, into the numerical recipe we use. The principal unrealistic assumptions we make are those of uniform mass density and incompressibility, a scalar valued Newtonian viscosity, a scalar valued electrical conductivity, and the omission of a finite thermal conductivity (it will be seen that in effect an infinite thermal conductivity has been assumed, since no thermal effects are allowed to develop except those associated with the incompressible velocity field). Despite what appear to be these gross oversimplifications of the physics of realistic toroidal machines such as tokamaks and RFPs, what remains is at the very perimeter of what is computable if we intend to stay with arbitrary initial configurations which are not in equilibrium, and to follow through with enforcing viscous boundary conditions. In this manuscript, we take into account fully three-dimensional time-dependent dynamics. The earlier papers assumed axisymmetry and time independence,[1,2] whereas in the present work we follow the relaxation evolution with a time-dependent three-dimensional code. This code has been described and benchmarked in Ref. 3.

What is of particular interest is the spontaneous development of both toroidal and poloidal rotations of the bulk magnetofluid as a whole. It is not physically obvious that this should happen, even though it has been known for some time to occur in toroidal laboratory devices.[4] The importance of non-zero velocities in the MHD description of toroidally confined plasma was realized by Pfirsch and Schlüter,[5] however without taking into account all the different terms in the force balance. We will take into account all these terms. We also mention that gyrokinetic simulations are able to reproduce transport levels in the core plasma of tokamaks but there is not yet a clear explanation of the toroidal rotation measured in such devices. For a comprehensive review in gyrokinetics that shows the advances in this subject, we refer to Ref. 6, and references therein. In Refs. 7–9, velocity fields generated by MHD effects were also investigated, but taking into account several additional refinements of the description. Here, we use a simple model allowing larger parametric studies where we can disentangle the influence of the control parameters and the considered geometry. The degree of the two types of rotation are seen to depend upon several things, such as the Reynolds-like dimensionless numbers assumed for the magnetofluid; the geometry of the toroid, which is allowed to have variable cross sections and the safety factor of the magnetofluid.

The numerical technique employed is relatively recent, and descends from what has been called the volume penalization technique,[10] originally developed for hydrodynamics.

a)jorge.a.morales@outlook.com

 

The entire computational domain is assumed to be three-dimensional and spatially periodic, so that pseudospectral methods can be employed, taking advantage of the fast Fourier transform and eliminating some complications associated with imposing incompressibility of the velocity and magnetic fields. Then, a toroidal volume is carved out within the volume of one period in each direction. Inside the toroid, the transport coefficients of viscosity and resistivity are assumed small but non-zero. Outside the toroid, mechanical and magnetic activities are suppressed using the penalization technique.[11] A steep gradient between the two regions serves as an active viscous boundary. The method has been used to considerable effect both for Navier-Stokes turbulence[12] and for magnetofluids in the recent past.[3,11,13] The Fourier pseudo-spectral codes used for the dynamical advancement of the field quantities are of a well-studied type.

In Sec. II, we fix the geometry of the confined magnetofluid and write down the system of equations and boundary conditions that will govern the dynamics. An external forcing of the magnetic field provides the toroidal electric field which initiates and drives the current. A vacuum toroidal dc magnetic field, regarded as externally supported from outside the system, is also assumed to be present. In addition, another toroidal component of the magnetic field is allowed to develop in time if the dynamics so dictate.

In Sec. III, the results are presented. They are divided in four different parts. The first discusses the generation of toroidal velocities for a strongly diffusive system. The second exposes the results where the nonlinear term is dominant and a comparison is made between different toroidal geometries. In the third section, we study the effect of the variation of the safety factor and in the last part how the system evolves if the imposed toroidal magnetic field is inverted. We illustrate in detail the development of the driven magnetofluid configurations and the development of spontaneous toroidal rotation.

## II. GEOMETRICAL CONFIGURATION AND GOVERNING EQUATIONS

In the MHD approximation, the plasma is described as a charge-neutral conducting fluid. Despite its low complexity compared to kinetic descriptions, it can give rise to a wealth of intricate phenomena and its analytical treatment is only possible in some simplified cases, either in the absence of velocity fields[14,15] or in the absence of non-linear interactions.[16] If one considers the complete problem, one necessarily needs to consider a numerical discretized approximation of the full nonlinear system. The equations we consider are the dimensionless incompressible viscoresistive MHD equations for the velocity field $\boldsymbol{u}$ and for the magnetic field $\boldsymbol{B}$, in "Alfvénic" units[2]

$$\frac{\partial \boldsymbol{u}}{\partial t} - M^{-1}\nabla^2 \boldsymbol{u} = -\nabla\left(P + \frac{1}{2}u^2\right) + \boldsymbol{u}\times\boldsymbol{\omega} + \boldsymbol{j}\times\boldsymbol{B}, \quad (1)$$

$$\frac{\partial \boldsymbol{B}}{\partial t} = -\nabla\times\boldsymbol{E}, \quad (2)$$

$$\boldsymbol{E} = S^{-1}\boldsymbol{j} - \boldsymbol{u}\times\boldsymbol{B}, \quad (3)$$

$$\nabla\cdot\boldsymbol{u} = 0, \quad \nabla\cdot\boldsymbol{B} = 0, \quad (4)$$

with the current density $\boldsymbol{j} = \nabla\times\boldsymbol{B}$, the vorticity $\boldsymbol{\omega} = \nabla\times\boldsymbol{u}$, the pressure $P$, and the electric field $\boldsymbol{E}$. These equations are non-dimensionalized using the toroidal Alfvén speed $C_A = B_{ref}/\sqrt{\rho\mu_0}$ as typical velocity, with $B_{ref} = 1.2$ the reference toroidal magnetic field at the center of the torus ($R = R_0 = 0.55\pi \approx 1.73$ for both considered geometries), $\rho$ the density that is considered constant in the present study, and $\mu_0$ the magnetic permeability. We will exclusively consider two toroidal geometries with differently shaped cross-sections (see Fig. 1). The reference length $L$ is the diameter of the cross section for the circular case and is the minor diameter for the asymmetric "D" shape ($L = 0.6\pi \approx 1.88$ for both geometries). The "D" shape parametric equation is a modified version of the formula given by Manickam[17]

$$R(t) = R_0 + \frac{L}{2}\left[\cos(t - \alpha + \delta\sin(t))\cos(\zeta) - \kappa\sin(t)\sin(\zeta)\right], \quad (5)$$

$$Z(t) = \frac{L}{2}\left[\cos(t - \alpha + \delta\sin(t))\sin(\zeta) + \kappa\sin(t)\cos(\zeta)\right], \quad (6)$$

with $t \in [0, 2\pi]$, $\delta$ the triangularity, $\kappa$ the ellipticity, $\alpha$ the asymmetry, and $\zeta$ the rotation angle. For the considered asymmetric cross section, the following values of these parameters are chosen: $\delta = 0.5$, $\kappa = 2.1$, $\alpha = 0.4$, and $\zeta = 0.15$.

The MHD equations are completed by the initial and boundary conditions of the problem, and two dimensionless quantities: the viscous Lundquist number ($M$) and the Lundquist number ($S$) defined as

$$M = \frac{C_A L}{\nu}, \qquad S = \frac{C_A L}{\lambda}, \quad (7)$$

with $\lambda$ the magnetic diffusivity and $\nu$ the kinematic viscosity. The ratio of these two quantities is the magnetic Prandtl number $Pr = \nu/\lambda$, which we have chosen unity in the present study, thereby reducing the number of free parameters, which characterize the magnetofluid, to one, the viscous Lundquist number, $M$. Previous investigations indicate that it is the Hartmann number which is proportional to the

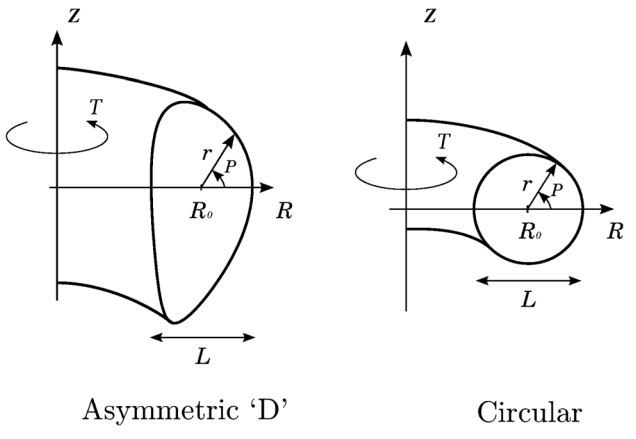


FIG. 1. Cross-sections of the toroidal geometries considered in the present work. The toroidal direction is labelled $T$ and the poloidal $P$.

geometric mean of the viscosity and the magnetic diffusivity which is important to the dynamics.[18,19] In setting the Prandtl number to one, a change in the viscous Lundquist numbers, $M$ or $S$, is equivalent to a change in the Hartmann number.

In the ideal MHD framework, a scalar-pressure equilibrium state is assumed in which $\boldsymbol{u} = 0$

$$\boldsymbol{j} \times \boldsymbol{B} = \nabla P. \tag{8}$$

This equilibrium is possible in a cylindrical geometry, for instance in $z$- and $\theta$-pinches. It is shown in Refs. 20 and 21 that in the case of finite conductivity such an equilibrium is not possible in a toroidal geometry if irrotational toroidal magnetic and electric fields are applied, as will be the case in the present study. We assume the toroidal electric field to be created by a central solenoid situated along the $Z$ axis, generating a time-proportional magnetic flux in the $Z$ direction, $\Phi_B \sim t$. Using Faraday's law, we have

$$\oint \boldsymbol{E} \cdot d\boldsymbol{l} = -\frac{\partial \Phi_B}{\partial t} = \text{constant}, \tag{9}$$

where the line-integral is chosen along a toroidal loop. The integration of the toroidal electric field on a toroidal loop is thus constant, and consequently the imposed toroidal electric field profile in our investigation is $E_{0_T}(R) \propto 1/R$. In the simple case of a space-uniform conductivity, which we consider in the present study, the current density has the same dependence. The form for the imposed toroidal magnetic field, which is also proportional to $1/R$, comes from the integration of Ampère's law on a toroidal loop. So, the externally imposed magnetic field and toroidal, laminar, and voltage-driven current density are given by

$$\boldsymbol{B}_{0_T}(R) = \mathcal{C}\frac{R_0}{R}\boldsymbol{e}_T, \qquad \boldsymbol{j}_{0_T}(R) = \mathcal{D}\frac{R_0}{R}\boldsymbol{e}_T. \tag{10}$$

All the calculations are performed using these prescribed $\boldsymbol{B}_{0_T}$ and $\boldsymbol{j}_{0_T}$. The parameter $\mathcal{D} = 0.5$ for all the simulations presented in this paper and $\mathcal{C} = 1.2$ for the cases presented in Secs. III A and III B. In Sec. III C, the $\mathcal{C}$ parameter is varied (this changes the safety factor) it takes the values $\{1.2, 1.0, 0.8, 0.6\}$. In the last part (Sec. III D) the toroidal field is reversed $\mathcal{C} = -1.2$. The toroidal magnetic and current density profiles give the imposed three-dimensional helical magnetic field $\boldsymbol{B}_0 = \boldsymbol{B}_{0_T} + \boldsymbol{B}_{0_{pol}}$, with $\boldsymbol{B}_{0_{pol}} = B_{0_R}\boldsymbol{e}_R + B_{0_Z}\boldsymbol{e}_Z$. The poloidal magnetic field is calculated from the current density distribution $\boldsymbol{j}_{0_T}(R)$. For the details of generating the poloidal magnetic field in general geometries numerically we refer to the Appendix. Here, $\boldsymbol{e}_T$, $\boldsymbol{e}_R$, and $\boldsymbol{e}_Z$ are unit vectors in the toroidal/azimuthal, radial, and vertical directions, respectively (Fig. 1).

The toroidal magnetic field magnitude is tuned to have an edge magnetic surface averaged safety factor $q_e = 1/2\pi \oint B_{0_T}|_e/(RB_{0_P})|_e ds = 6.1$ for the asymmetric geometry and $q_e = 3.6$ for the symmetric cross section, with $s$ the poloidal direction along a magnetic surface.[22] These safety factor values will be used for the majority of the studied cases. The pinch-ratio associated to these values of $q_e$, defined as the ratio between the wall-averaged poloidal and the volume-averaged toroidal imposed magnetic field, $\Theta = \overline{B_{0_P}}/\langle B_{0_T}\rangle = 0.16$, is the same for both geometries. A bar over a symbol indicates an average over the entire boundary. The typical safety factor profiles considered in the present study are presented in Fig. 2.

The Lorentz force resulting from the calculated poloidal field $\boldsymbol{B}_{0_{pol}}$ and the imposed toroidal current density $\boldsymbol{j}_{0_T}$ is not curl-free.[20,21] Since the curl of a pressure gradient is necessarily zero, the equilibrium described by (8) becomes impossible and additional terms of Eq. (1) need to be taken into account to balance the equation. Since all other terms in (1) are proportional to (or quadratic in) the velocity, the resulting state must be dynamic. In other words if we take the curl of Eq. (1) we end with the vorticity equation

$$\frac{\partial \boldsymbol{\omega}}{\partial t} - M^{-1}\nabla^2\boldsymbol{\omega} - \nabla \times (\boldsymbol{u} \times \boldsymbol{\omega}) = \nabla \times (\boldsymbol{j} \times \boldsymbol{B}) \neq 0, \tag{11}$$

we observe that if the Lorentz force term is not curl-free, it acts as a source of vorticity: a toroidal plasma, described by viscoresistive MHD, confined by curl-free toroidal electric and magnetic fields, necessarily moves.

It is true that the rationale described above depends on the choice of the electric conductivity, which was assumed to be uniform. It was however shown[23] that to satisfy (8) in a torus, very unusual profiles of the electrical conductivity must be assumed. The simple case of constant magnetic resistivity is then treated in this study. The case of non-uniform resistivity profiles is one of our most important goals.

We will rephrase this, since it is the key message of the present work. In order to generate a helically twisted magnetic field, as needed in toroidally confined plasmas one needs to induce a toroidal current through the plasma. In ideal MHD equilibrium theory, this current can be chosen in such a way that it satisfies the equilibrium condition, Eq. (8). Indeed, in ideal MHD, Ohm's law simplifies to

$$\boldsymbol{E} = -\boldsymbol{u} \times \boldsymbol{B} \tag{12}$$

and the direct link between the electric field and the current density disappears. In the resistive MHD context, for a

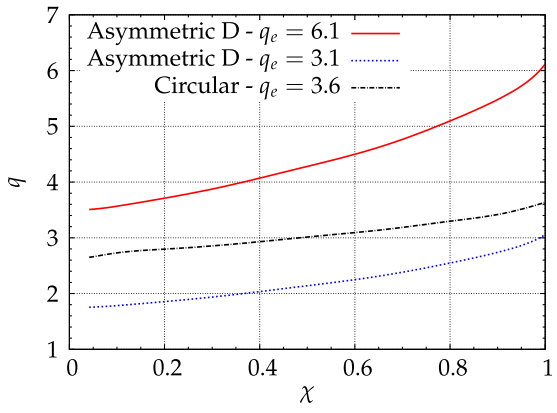


FIG. 2. Safety factor profiles as a function of the poloidal magnetic flux function $\chi$ (defined in the Appendix). For the asymmetric geometry, the typical and the smallest profile assessed in Sec. III C are presented. For the symmetric case, a single profile is considered.

given imposed electric field, the toroidal current density cannot be freely chosen, but is given by the imposed toroidal electric field. If this current, combined with the imposed toroidal magnetic field does not yield a Lorentz force which is balanced by the pressure gradient, the plasma will accelerate and adjust towards a dynamic equilibrium. We note that if we drop the assumption that the electric field is given *a priori* by a physical mechanism (such as the induction by a central solenoid), it is possible to obtain a static equilibrium by adjusting *a posteriori* the electric field (see, for instance, the review article[24]), but this is not the case we consider. In other words, in resistive MHD, for a given electric field it is not possible to correct for an imbalance in $\boldsymbol{j}\times\boldsymbol{B}=\nabla P$, self-consistently without having a non-zero velocity.

It follows from the foregoing that it is necessary to take into account all other terms in the MHD equations, and analytical treatment becomes impossible unless symmetries are assumed. To study the full dynamics, we are obliged to solve numerically the system and this is what is done in the present investigation. Equations (1)–(4) are discretized with a Fourier pseudo-spectral method on a Cartesian grid. To impose the boundary conditions, we use the volume-penalization technique, a method of the immersed boundary type. Results for two-dimensional viscoresistive MHD can be found in Refs. 11 and 13. The method is presented in detail for three-dimensional viscoresistive MHD equations in Ref. 3. The study exposed in the present paper is the numerical study of confined MHD using the toroidal geometries shown in Fig. 1.

The total magnetic and current density fields are decomposed into a base component and a perturbation

$$\boldsymbol{B}=\boldsymbol{B}_0+\boldsymbol{B}' \quad \text{and} \quad \boldsymbol{j}=\boldsymbol{j}_0+\boldsymbol{j}'. \tag{13}$$

Numerically only the perturbation of the magnetic and current density field are computed, the base magnetic field, $\boldsymbol{B}_0$ and current density $\boldsymbol{j}_0$, computed from (10), are fixed. Note that the base current density field is only in the toroidal direction ($\boldsymbol{j}_0=\boldsymbol{j}_{0_T}$) and the base magnetic field is in the toroidal and poloidal directions ($\boldsymbol{B}_0=\boldsymbol{B}_{0_T}+\boldsymbol{B}_{0_{pol}}$). These base fields are introduced in the Navier-Stokes equation and in the induction equation as follows:

$$\frac{\partial \boldsymbol{u}}{\partial t}-M^{-1}\nabla^2\boldsymbol{u}=-\nabla\left(P+\frac{1}{2}u^2\right)+\boldsymbol{u}\times\boldsymbol{\omega}+\left(j'+j_0\right)\times\left(\boldsymbol{B}'+\boldsymbol{B}_0\right) \tag{14}$$

$$\frac{\partial \boldsymbol{B}'}{\partial t}-S^{-1}\nabla^2 B'=\nabla\times[\boldsymbol{u}\times(\boldsymbol{B}'+\boldsymbol{B}_0)], \tag{15}$$

with $\boldsymbol{j}'=\nabla\times\boldsymbol{B}'$. Note that $\boldsymbol{j}_0=\boldsymbol{j}_{0_T}=\nabla\times\boldsymbol{B}_{0_{pol}}$ and $\nabla\times\boldsymbol{B}_{0_T}=0$. To close the equations, we have the incompressibility of the velocity field and the solenoidal constraint on the magnetic field

$$\nabla\cdot\boldsymbol{u}=0, \qquad \nabla\cdot\boldsymbol{B}=0. \tag{16}$$

The boundary conditions are to be no-slip, $\boldsymbol{u}|_{wall}=0$, for the velocity. For the magnetic perturbation, the poloidal component and the component normal to the wall vanish, $B'_{P//_{wall}}=B'_{\perp_{wall}}=0$, while the toroidal component is free. The normal component $B_\perp$ vanishing at the wall physically corresponds to perfectly conducting boundary conditions. The zero poloidal fluctuations $B'_{P//_{wall}}$ are imposed for numerical convenience. Since the perturbed magnetic field remains small compared to the field $\boldsymbol{B}_0$ in the present investigation, we do not think that this simplification significantly influences the results.

The initial condition for the simulations is zero magnetic perturbations and zero velocity. The simulations are carried out on a cubic domain of size $(2\pi)^3$ for the asymmetric and $(2\pi\times 2\pi\times\pi)$ for the symmetric cross section consisting of $256^3$ grid points. We fix the penalization parameter to $\eta=5\times10^{-4}$. The time step is adaptive and the chosen CFL coefficient is 0.1.

## III. RESULTS AND DISCUSSION

The results are divided into four different parts. The first shows the solution of the simulations at a low viscous Lundquist number, where an illustration of the generation of toroidal velocities is presented. The second exposes the calculations at higher viscous Lundquist, where the flow behavior of the plasma changes towards a dominantly toroidal flow. In the third section, we compare, at fixed transport coefficients, simulations carried out for different safety factors; and in the fourth section, we show the results when the toroidal magnetic field is reversed.

### A. Generation of toroidal velocities at low viscous Lundquist number

In this section, the calculations are performed for a low viscous Lundquist number, $M=23$, in the geometry with symmetric cross section and $q_e=3.6$. All the results are presented when the system has reached a statistically stationary state.

Fig. 3 shows the presence of a poloidal flow, a pair of counterrotating vortices in the poloidal plane. In this case, the flow topology is almost axisymmetric with respect to the $Z$-axis. To visualize more clearly, the toroidal velocities and the double poloidal recirculation, the azimuthally averaged velocity field is presented in Fig. 4. We distinguish four different zones, where the toroidal velocity changes sign, and the already mentioned "double smoke ring." Indeed, in the limit of vanishing nonlinearity, Bates and Montgomery[16] showed

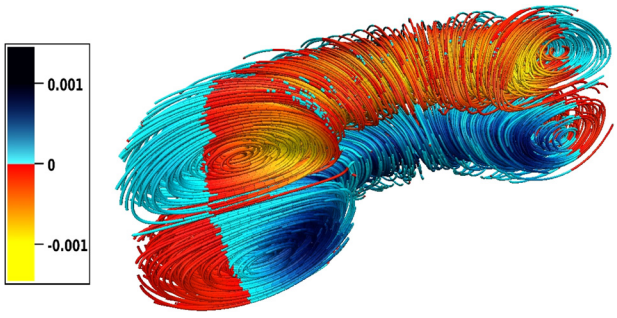


FIG. 3. Streamlines colored with toroidal velocity ($u_T$) for $M=23$.

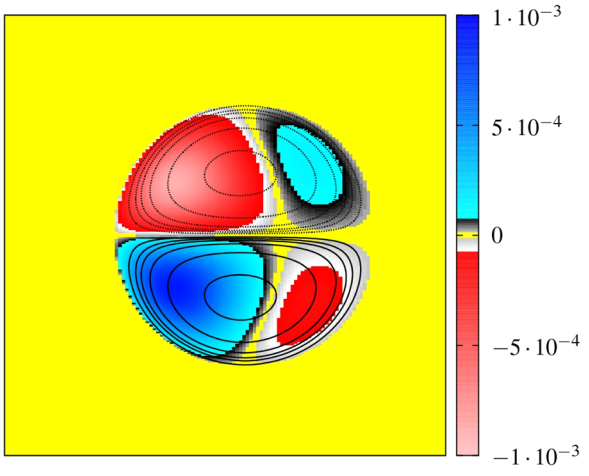


FIG. 4. Azimuthally averaged toroidal velocity and poloidal stream function contours (solid line positive, dotted line negative contours).

analytically that the steady state solution is a pair of poloidally rotating vortices, aligned with the toroidal direction.

The origin of toroidal velocities was demonstrated for vanishing viscous Lundquist in a rectangular cross section.[1,25] For a circular cross section and at low $M$ number, we will illustrate the generation of this velocity component. First, we illustrate that the forcing appearing in the vorticity equation (11) creates two toroidal cells with opposite values of the vorticity in the torus. These cells are symmetric with respect to the mid-plane of the torus (see Fig. 5(a)). This creates automatically a radial velocity that will interact with the imposed toroidal magnetic field (Fig. 5(b)). The interaction will produce a perturbation to the toroidal magnetic field ($B'_T$). Notice that this magnetic field will have positive and negative areas located in a similar position as the radial velocity (Figs. 5(b) and 5(c)). It was shown[25] that the equation giving the first order perturbed toroidal magnetic component $B_T^{\prime(1)}$ is

$$\nabla^2\left(B_T^{\prime(1)}\boldsymbol{e}_T\right) \sim -u_R\frac{B_{T_{ref}}}{R^2}\boldsymbol{e}_T. \tag{17}$$

The sign of the right hand side will only depend on the sign of $u_R$ and of the imposed toroidal field $B_{T_{ref}}$.

It follows that the curl of the perturbed toroidal magnetic field ($B'_T$) will produce a poloidal current density, $\boldsymbol{j}'_{pol} = \nabla \times B'_T$ (Fig. 6(a)). The imposed poloidal magnetic field $\boldsymbol{B}_{0_{pol}}$ will then interact with the perturbed current density $\boldsymbol{j}'_{pol}$ to create a toroidal Lorentz force (see Figs. 6(b) and 6(c)). The Lorentz force will finally induce toroidal velocities. Note that there is a similarity in the negative and positive zones between the toroidal velocity and the toroidal Lorentz force fields (see Figs. 4 and 6(c)). We note that the sign in the toroidal Lorentz force depends exclusively on the angle between $\boldsymbol{j}'_{pol}$ and $\boldsymbol{B}_{0_{pol}}$. As a consequence, this angle influences directly the toroidal velocity direction.

Another way, to understand the fact that the poloidal flow interacts first with the magnetic field creating subsequently toroidal velocities is to see the time evolution of the different velocity components. The velocities in the poloidal plane (in the poloidal direction $P$ and in the minor radius direction $r$) grow first. After that the toroidal velocity is generated (see Fig. 7).

At low viscous Lundquist number, the dominant velocities are in the poloidal plane and form two counterrotating vortices. Small toroidal velocities appear and they form a quadrupole with alternating positive and negative directions. The analytical results published by Bates and Montgomery[16] are in good agreement. Also the numerical generation of toroidal velocities agrees with the calculations made by Kamp and Montgomery.[1]

### B. Simulations for higher viscous Lundquist numbers

In this section, the calculations are made for the asymmetric cross section with fixed $q_e = 6.1$ and for the circular cross section, $q_e = 3.6$. The viscous Lundquist numbers are modified changing the transport coefficients $\nu$ and $\lambda$ (with $Pr = 1$), keeping the geometry and the reference toroidal magnetic field unchanged, $B_{ref} = 1.2$.

With higher viscous Lundquist numbers, it takes longer for the system to reach the saturated state. In the first instants an oscillatory behavior is present (see, for example, the different energy evolutions in Figs. 8 and 9). The kinetic and the fluctuating magnetic energy oscillate in opposition of phase, but these oscillations are damped out in a finite time. In the following section, we will analyse and compare the different simulations when the system has reached this non-oscillatory steady state.

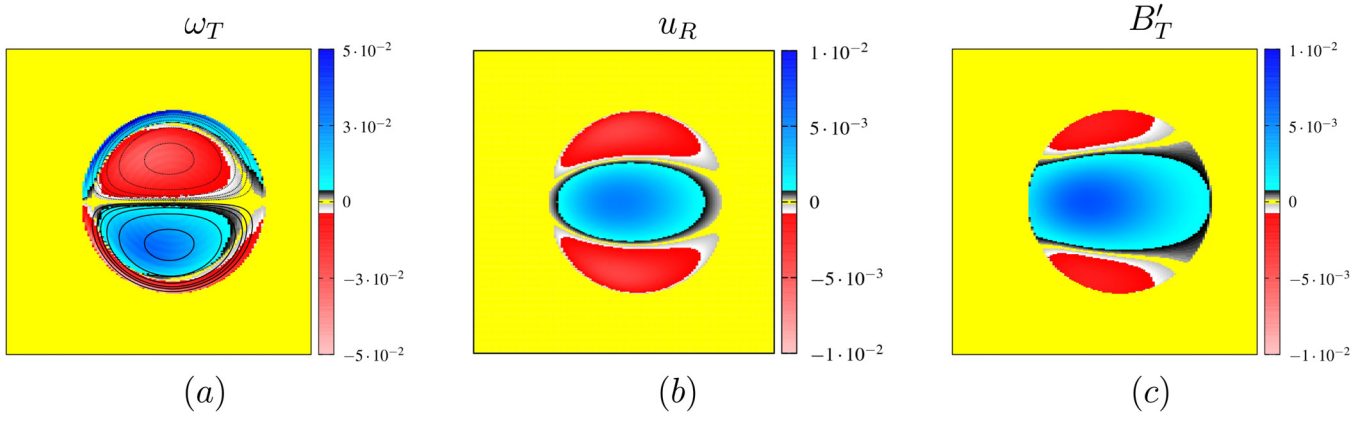


FIG. 5. Azimuthally averaged: (a) Toroidal vorticity $\omega_T$ and poloidal stream function, (b) radial velocity $u_R$, and (c) perturbation of the toroidal magnetic field, $B'_T$.

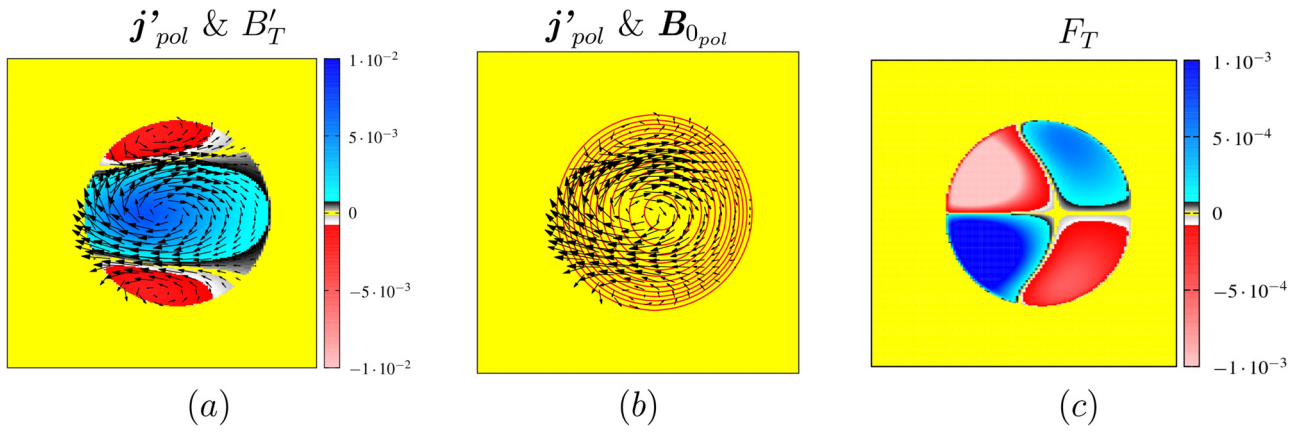


FIG. 6. Azimuthally averaged: (a) Poloidal current density $\boldsymbol{j}'_{pol}$ (vectors) and perturbation of the toroidal magnetic field $B'_T$, (b) current density $\boldsymbol{j}'_{pol}$ (vectors) and imposed poloidal magnetic field lines $\boldsymbol{B}_{0_{pol}}$, and (c) toroidal Lorentz force $F_T$.

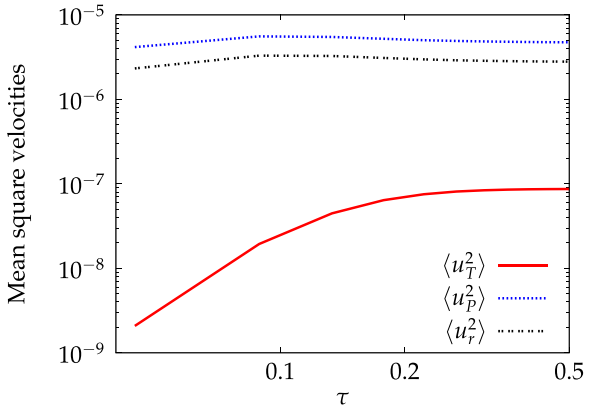


FIG. 7. Poloidal and toroidal square velocity component evolutions at early times, in toroidal Alfvénic time units ($\tau$).

The calculations with increasing viscous Lundquist number show an important change in the fluid flow. The previously small toroidal velocities increase considerably and will become more important, in magnitude, than the poloidal plane velocities. For nonzero nonlinearity, i.e., by increasing $M$, the vortices start moving in the toroidal direction. The toroidal velocity increases with $M$ in the two considered geometries. The three-dimensional velocity streamlines show a substantial change of topology, from dominantly poloidal to dominantly toroidal flow (see Figs. 10 and 11).

The flow evolution is quantified in Fig. 12, where we observe that the principal direction of the flow is toroidal if $M$ is raised beyond ~40. The square toroidal velocity saturates for increasing $M$ at a value of ~80% of the total square velocity for the asymmetric cross section and at ~60% for the circular profile. This toroidal organization of the flow is consistent with the tendency of the velocity field to align with the magnetic field, as illustrated in Fig. 13, where we compute the average (over the toroidal domain) of the absolute value of the cosine of the angle between the velocity and magnetic field. This quantity is equal to one if the velocity and the magnetic field are perfectly aligned or antialigned. The evolution of the ratio $\langle u_T^2\rangle/\langle|\boldsymbol{u}^2|\rangle$ with $M$ shows the same trend as the alignment between the magnetic and the velocity field.

An important difference is observed between the flows that are generated in the two geometries. The volume averaged toroidal angular momentum is defined by

$$\langle L_T\rangle = \frac{1}{V}\int_V Ru_T dV. \tag{18}$$

For the torus with circular cross section, this quantity is zero to a good computational approximation ($<10^{-15}$). The up-

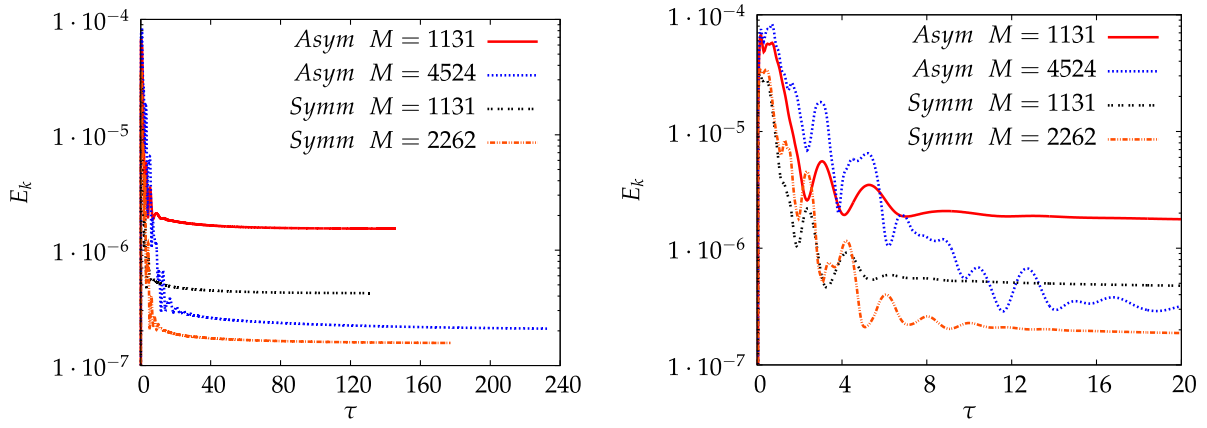


FIG. 8. Kinetic energy evolution at large times (left) and oscillatory behavior at early time (right) in toroidal Alfvénic time units, for asymmetric and symmetric geometry.

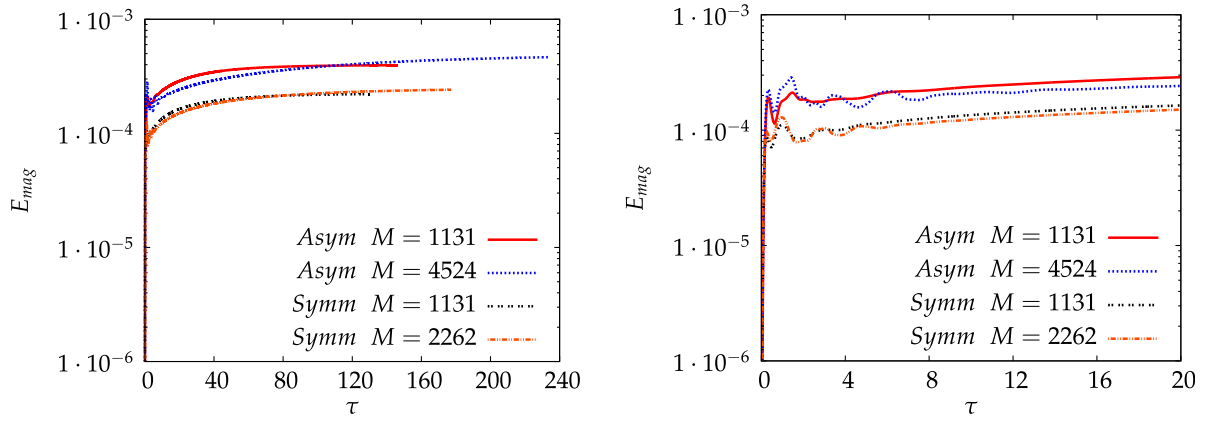


FIG. 9. Fluctuating magnetic energy evolution at large times (left) and oscillatory behavior at early time (right) in toroidal Alfvénic time units, for asymmetric and symmetric geometry.

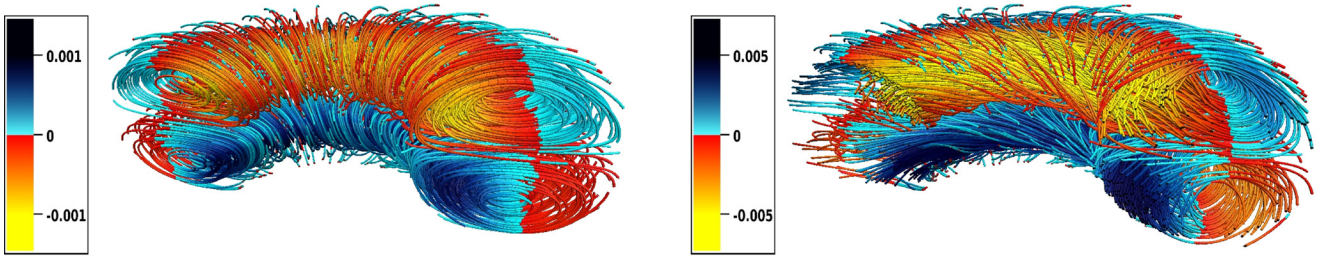


FIG. 10. Streamlines colored with toroidal velocity ($u_T$) for $M = 23$ (left) and $M = 226$ (right) for the symmetric torus.

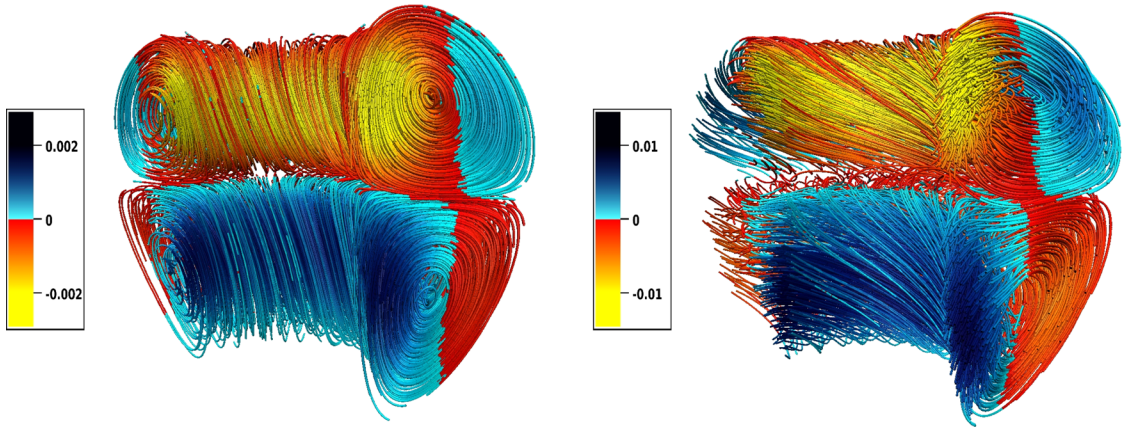


FIG. 11. Streamlines colored with toroidal velocity ($u_T$) for $M = 23$ (left) and $M = 226$ (right) for the asymmetric torus.

down anti-symmetry of the velocity field is responsible for this absence of toroidal angular momentum. However, for the torus with asymmetric cross section this is not the case. There is a symmetry breaking of the flow and the volume integral of the toroidal velocity is nonzero. In our calculations, this can be visualized in the azimuthally averaged velocity fields in Fig. 14. It is more clear for the last case, at $M = 4524$, that the positive toroidal velocity occupies a larger part of the poloidal plane than the negative toroidal velocity. To quantify the amount of dissymmetry in the flow, we present the evolution of the normalized toroidal angular momentum with $M$ (see Fig. 15). To normalize, we use the RMS toroidal angular momentum defined by $L_{T_{rms}} = \sqrt{\langle (Ru_T)^2 \rangle}$. The normalized toroidal angular momentum increases with the viscous Lundquist number. This up-down asymmetry effect is in agreement with time-independent computations[2] and also with gyrokinetic simulations and experiments.[26,27] At the steady state, the volume averaged toroidal angular momentum is given by the balance between the toroidal Lorentz force in the torus volume and the viscous dissipation at the torus wall, the other terms in the momentum equation vanish if we consider no-slip boundary conditions and $\boldsymbol{B} \cdot \boldsymbol{n} = 0$. The volume integral of the momentum equation projected in the toroidal direction at the steady state writes

$$\iint_S M^{-1} \nabla u_T \cdot \boldsymbol{n} dS + \iiint_V (\boldsymbol{j}'_{pol} \times \boldsymbol{B}_{0_{pol}}) \cdot \boldsymbol{e}_T dV = 0, \quad (19)$$

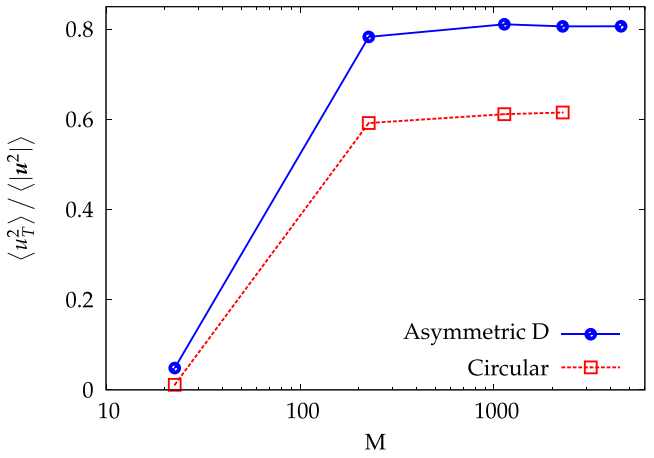


FIG. 12. The ratio of the mean-square toroidal velocity to the total mean-square $\langle u_T^2 \rangle / \langle |\boldsymbol{u}^2| \rangle$ as a function of $M$.

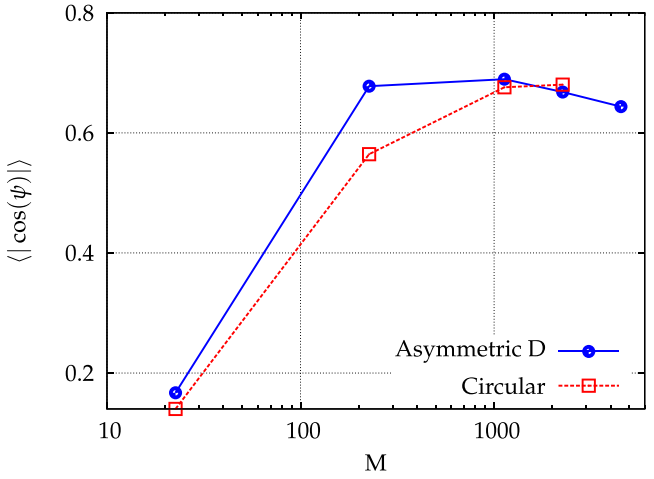


FIG. 13. Average over the domain of the absolute value of the cosine of the angle between the velocity field and magnetic field.

with $\boldsymbol{n}$ the vector normal to the wall. The viscosity dissipates the energy injected by the toroidal Lorentz force and a dynamic equilibrium is created. In the "D" shaped cross section there is an asymmetric Lorentz force inducing a finite

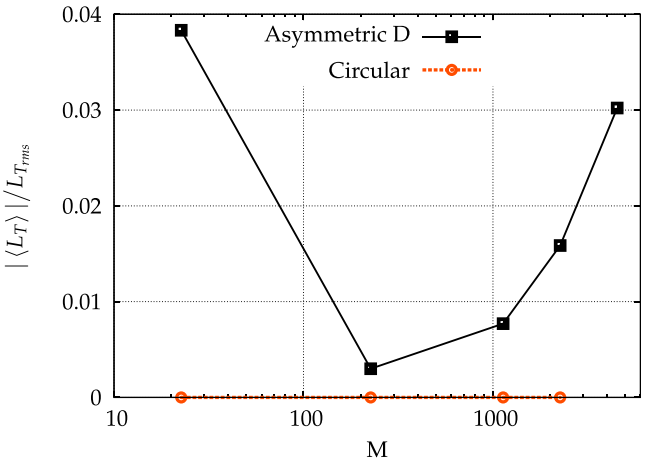


FIG. 15. Normalized toroidal angular momentum $|\langle L_T \rangle| / L_{T_{rms}}$ as a function of $M$ observed in the tori with asymmetric and symmetric cross section, respectively (left).

TABLE I. JET parameters.

| $B_{T_{ref}}$ | $\rho$ | $C_A$ | $R_0$ |
|---|---|---|---|
| 2.8 T | $1.2 \times 10^{-7}$ kg/m$^3$ | $7.2 \times 10^6$ m/s | 3 m |

volume averaged toroidal angular momentum. We recall that the generation of the toroidal Lorentz force creating the toroidal velocity is explained in Sec. III A and in Ref. 25.

Using typical JET tokamak parameters[28] (see Table I), the RMS toroidal rotation frequency for the highest Lundquist number in the asymmetric geometry is $f_{T_{rms}} = u_{T_{rms}}/R_0 \sim 1.42$ kHz. Note that the value of $S$ in experiments is several orders of magnitude higher and the aspect ratio (≈3 in JET and ≈1.8 in our study) is different, so that the toroidal rotation frequency value is not directly comparable to experimental observations.

Furthermore, in Fig. 14 we can observe the two counterrotating vortices. They are still present at higher viscous Lundquist but undergo a deformation and their center is shifted outwards. The larger toroidal velocities concentrate near the boundaries as well as the poloidal speeds (this can be seen

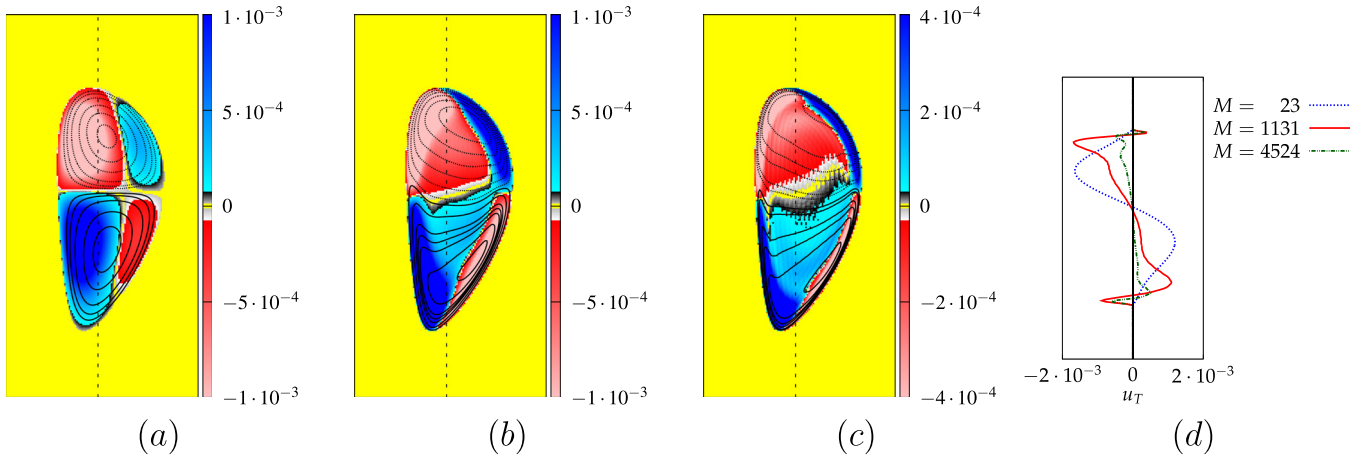


FIG. 14. Azimuthally averaged flow visualizations: toroidal velocity $u_T$ and poloidal stream function contours (solid line positive, dotted line negative contours) for $M = 23$ (a), $M = 1131$ (b), and $M = 4524$ (c). (d) Toroidal velocity profiles along a vertical cut. The position of these cuts is indicated in (a)–(c) by a dotted vertical line.

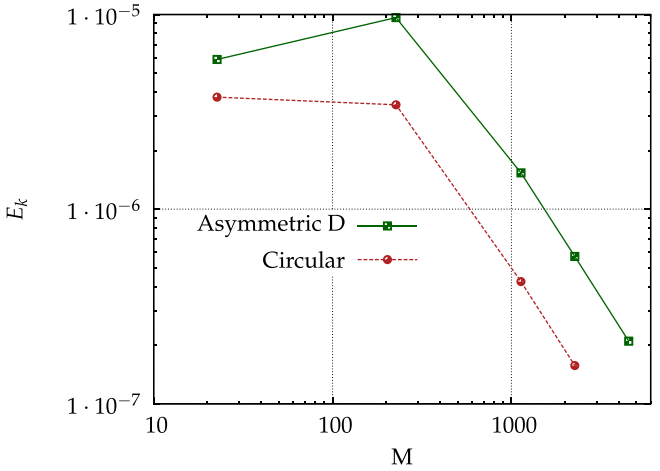


FIG. 16. Kinetic energy as a function of $M$ for the asymmetric and symmetric cross sections.

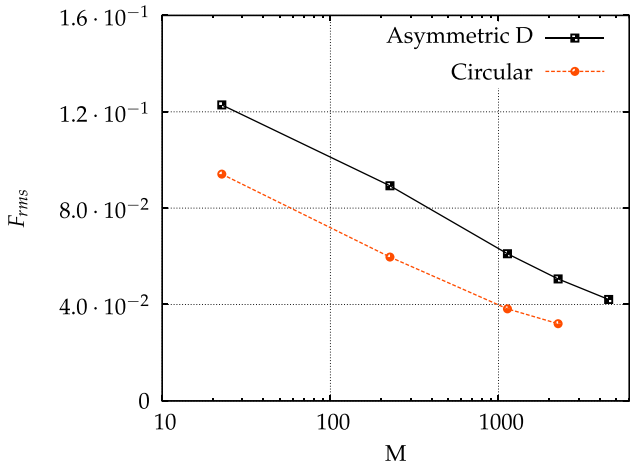


FIG. 17. Root mean square value of the Lorentz force as a function of the viscous Lundquist number.

from the stream function isocontours that tend to converge near the boundaries). Nevertheless, the velocity magnitude is globally less important for high $M$. In fact, the kinetic energy has a maximum and then decreases if the viscous Lundquist number is raised (see Fig. 16). This behavior is explained by the decrease of the magnitude of the Lorentz force with the viscous Lundquist number in the center of the domain. Indeed,

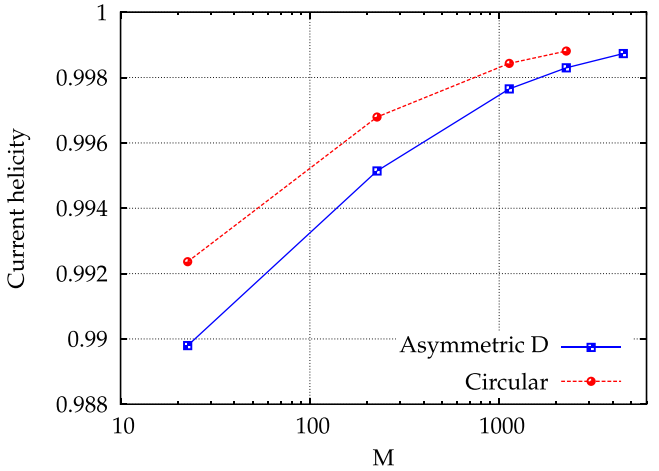


FIG. 19. Current helicity as a function of $M$ for the asymmetric and symmetric cross sections.

the plasma seems to self-organize to a state with a force-free region in the center, a behavior also observed for straight-cylinder computations at high pinch ratio.[29] The evolution with $M$ of the root mean square (RMS) value of this force is presented in Fig. 17. The spatial distribution of the norm of the Lorentz force vector in the poloidal plane is visualized for the asymmetric geometry in Fig. 18. The vanishing of the Lorentz force in the core comes from the alignment between the magnetic and current density fields. A measure giving the alignment between these three-dimensional quantities is the volume-averaged current helicity defined as

$$H_j = \left\langle \frac{\boldsymbol{j} \cdot \boldsymbol{B}}{\| \boldsymbol{j} \| \| \boldsymbol{B} \|} \right\rangle. \tag{20}$$

We observe (Fig. 19) that for increasing viscous Lundquist number the global current density and magnetic field tend to be oriented in the same direction, the quantity in the figure approaches the unit value. This causes the Lorentz force term to decrease for higher $M$ in the center of the domain, the magnitude of the imposed toroidal current density and magnetic fields remaining constant.

Mainly, the variation of the alignment between $\boldsymbol{j}$ and $\boldsymbol{B}$ occurs in the poloidal plane. To quantify the alignment among the poloidal current density and the poloidal magnetic

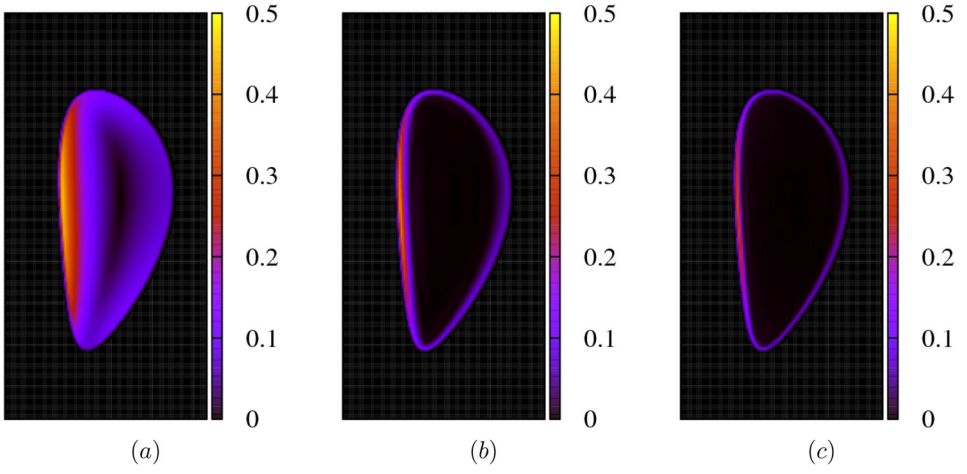


FIG. 18. Azimuthally averaged vector norm of the Lorentz force for $M = 23$ (a), $M = 1131$ (b), and $M = 4524$ (c).

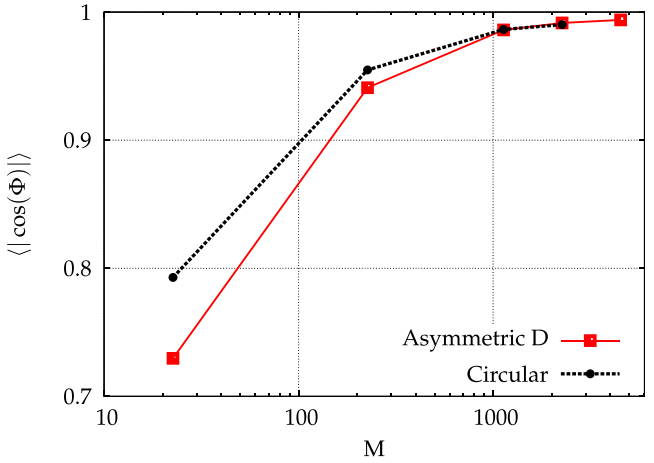


FIG. 20. Volume-averaged absolute value of the cosine of the angle between the poloidal current density ($\boldsymbol{j}_{pol}$) and the poloidal magnetic field ($\boldsymbol{B}_{pol}$) as a function of M.

field, we compute the volume-averaged absolute value of the cosine of the angle between these two fields

$$\langle|\cos\Phi|\rangle = \left\langle \frac{|\boldsymbol{j}'_{pol}\cdot\boldsymbol{B}_{pol}|}{\|\boldsymbol{j}'_{pol}\|\,\|\boldsymbol{B}_{pol}\|}\right\rangle, \tag{21}$$

where $\boldsymbol{j}'_{pol}$ and $\boldsymbol{B}_{pol}$ are the projections of $\boldsymbol{j}$ and $\boldsymbol{B}$ on the poloidal plane. This quantity at low viscous Lundquist is small compared to the value of the current helicity at the same $M$ number (see Figs. 19 and 20). With increasing viscous Lundquist, the cosine of this angle grows and approaches unity. There is a stronger change in the alignment between the current density and magnetic field in the poloidal plane. This poloidal alignment makes the toroidal Lorentz force vanish in the core of the domain.

Whether or not, the Lorentz force term reaches an asymptote at higher $M$ or if a transition to another state exists remains an open question.

The system is almost axisymmetric around $Z$ but small fluctuations around the toroidally averaged fields exist, defined as

$$\tilde{\boldsymbol{u}} = \boldsymbol{u} - \langle\boldsymbol{u}\rangle_T, \qquad \tilde{\boldsymbol{B}}' = \boldsymbol{B}' - \langle\boldsymbol{B}'\rangle_T. \tag{22}$$

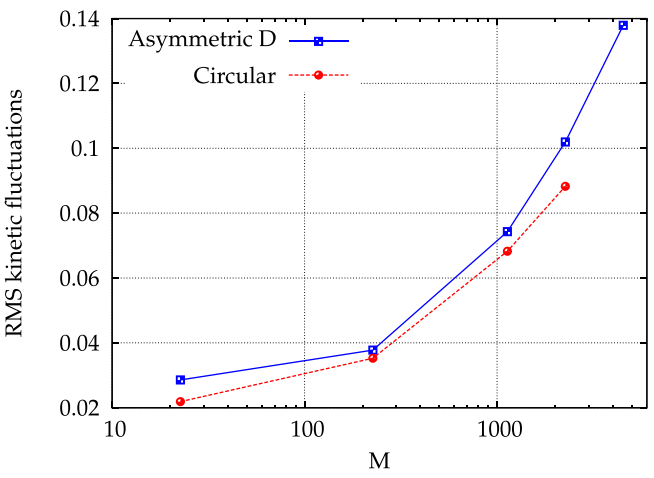


FIG. 21. RMS value of the non azimuthally symmetric velocity fluctuations, normalized by the total root mean square velocity.

The most important normalized fluctuations around the axisymmetric state are in the velocity field (Fig. 21), they are localized at the boundaries (see Fig. 23). The evolution of the normalized kinetic and magnetic fluctuations as a function of the viscous Lundquist number is presented, respectively, in Figs. 21 and 22. For the highest viscous Lundquist, $M = 4524$ and asymmetric cross section, we have the maximum ratio $\tilde{\boldsymbol{u}}_{rms}/\boldsymbol{u}_{rms} \sim 0.14$. The greatest normalized departure from axisymmetry for the perturbed magnetic field is also at $M = 4524$ for the "D" cross section, $\tilde{\boldsymbol{B}}'_{rms}/\boldsymbol{B}'_{rms} \sim 0.015$. In fact for the magnetic field, the fluctuations are of the same order of magnitude as the velocity field, but the magnitude of the perturbed magnetic field ($\tilde{\boldsymbol{B}}$) is larger, hence the normalized quantities are smaller. The distribution of the perturbations in the two-dimensional plane (Figs. 23 and 24) shows the velocity fluctuations mainly concentrated at the boundaries. These are the areas where the velocity is peaked (see, e.g., velocity profiles Fig. 14(d)) and where the velocity gradients are important. For the magnetic field, the fluctuations are spread in a larger region, they are more important at the high and low field side of the torus.

### C. Influence of the safety factor on the dynamics

The study of the influence of the safety factor $q_e$ is presented in this section where we consider only the asymmetric cross section geometry and the transport coefficients are kept constant ($\nu = \lambda = 2\times10^{-3}$). We recall that for all the simulations presented in this manuscript the magnetic Prandtl number is equal to one, $Pr = 1$. In this case, the viscous Lundquist number varies because the reference magnetic field used for its calculation is the imposed toroidal component and to modify the safety factor the magnitude of this field is changed, as also done in experiments.[30,31] The parameter $q_e$ takes four different values. We recall that this safety factor is defined as the ratio between the toroidal and poloidal imposed magnetic fields averaged over the magnetic surface at the edge of the toroidal domain

$$q_e = \frac{1}{2\pi}\oint\left.\frac{B_{0_T}}{(RB_{0_P})}\right|_e ds, \tag{23}$$

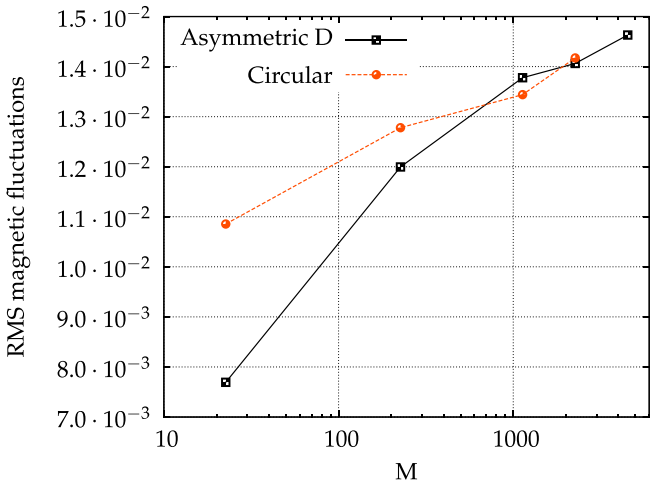


FIG. 22. RMS value of the non azimuthally symmetric magnetic fluctuations, normalized by the total root mean square perturbed magnetic field.

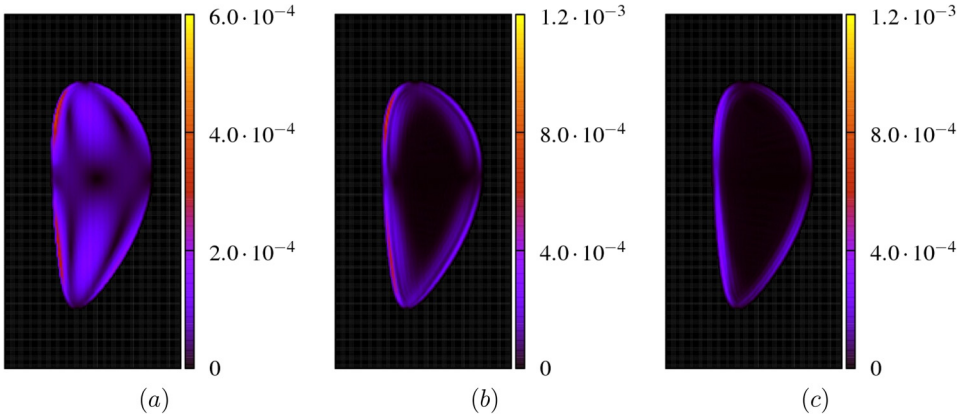


FIG. 23. Azimuthally averaged square velocity fluctuations around the azimuthal mean value for $M = 23$ (a), $M = 1131$ (b), and $M = 4524$ (c).

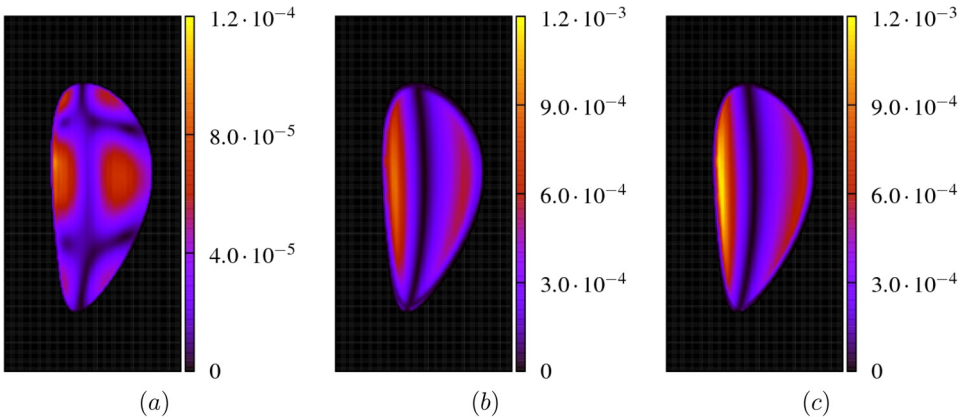


FIG. 24. Azimuthally averaged square magnetic fluctuations around the azimuthal mean value for $M = 23$ (a), $M = 1131$ (b), and $M = 4524$ (c).

TABLE II. Corresponding viscous Lundquist number for each safety factor value.

| $q_e$ | 6.1 | 5.1 | 4.1 | 3.1 |
|---|---|---|---|---|
| $M$ | 1131 | 942 | 754 | 565 |

with $s$ the poloidal direction along a magnetic surface.[22] The values of the viscous Lundquist number associated to each safety factor are presented in Table II.

The evolution of the total kinetic energy and the magnetic energy of the perturbation are similar for all studied cases (see Figs. 25 and 26). The main difference is the magnitude of the energies that is higher if the safety factor is small. At the steady state, the dependence of the kinetic energy on the safety factor is visualized in Fig. 27.

The growth of the kinetic energy with decreasing $q_e$ is in agreement with the reduction of the current helicity value (Fig. 28) corresponding to the fact that the Lorentz force term is stronger for a low safety factor. It is also observed

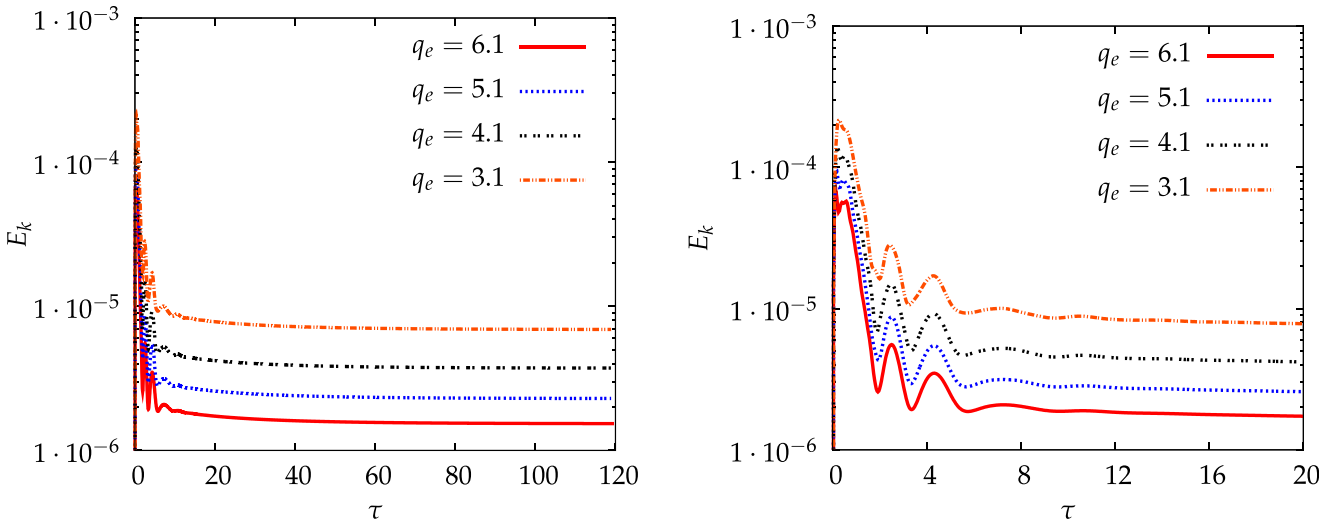


FIG. 25. Left: kinetic energy evolution. Right: a zoom on the early time instants. Time is given in toroidal Alfvénic time units.

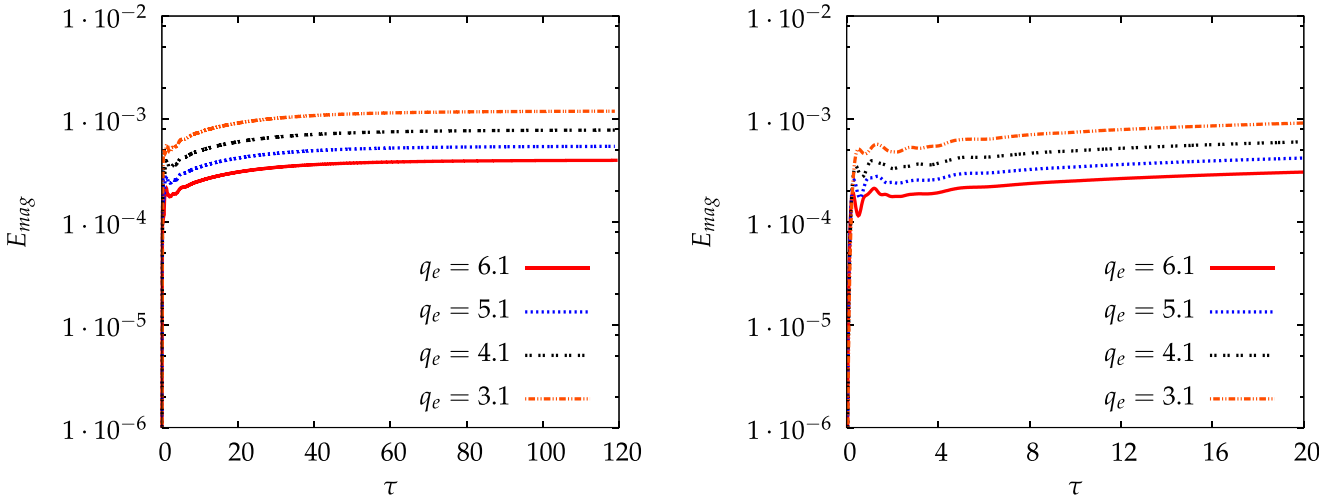


FIG. 26. Left: perturbed magnetic energy evolution. Right: a zoom on the early time instants. Time is given in toroidal Alfvénic time units.

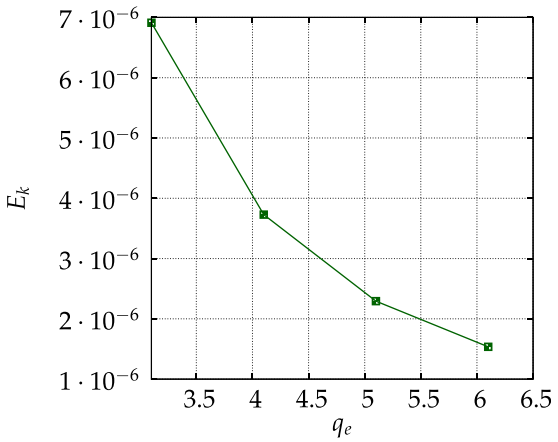


FIG. 27. Kinetic energy as a function of $q_e$.

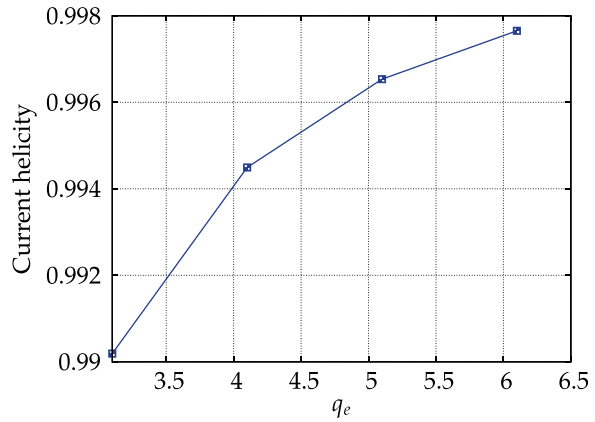


FIG. 28. Current helicity as a function of the safety factor $q_e$.

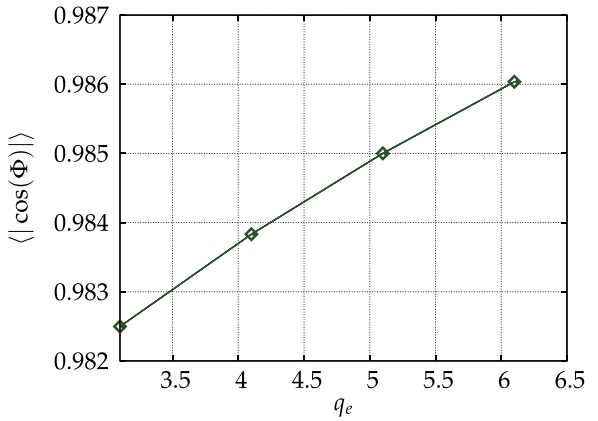


FIG. 29. Volume-averaged absolute value of the cosine of the angle between the poloidal current density ($\boldsymbol{j}_{pol}$) and the poloidal magnetic field ($\boldsymbol{B}_{pol}$) as a function of $q_e$.

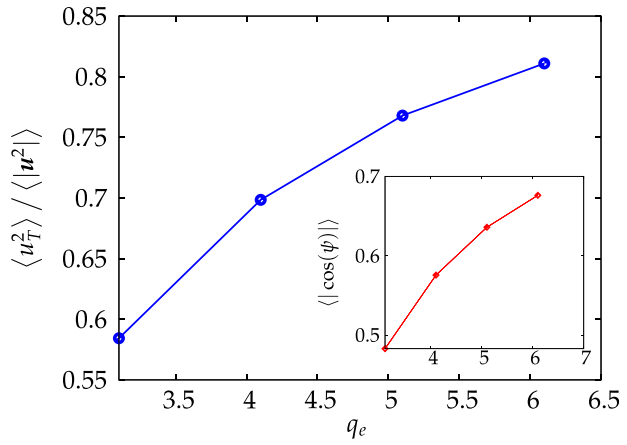


FIG. 30. The ratio of the mean-square toroidal velocity to the total mean-square $\langle u_T^2\rangle/\langle|\boldsymbol{u}^2|\rangle$ as a function of $q_e$. In the inset, we show the average over the domain of the absolute value of the cosine of the angle between the velocity field and magnetic field.

that in the toroidal direction the Lorentz force increases, since the alignment between the poloidal current density and the poloidal magnetic field is less important for small $q_e$ (Fig. 29). This variation is small compared to the variation caused by the modification of the transport coefficients, as shown in Sec. III B.

As in Sec. III B, the toroidal velocity dominates, but the ratio $\langle u_T^2\rangle/\langle|\boldsymbol{u}^2|\rangle$ decreases with decreasing $q_e$ (Fig. 30). Also the alignment between the magnetic and velocity field is less important (inset of Fig. 30).

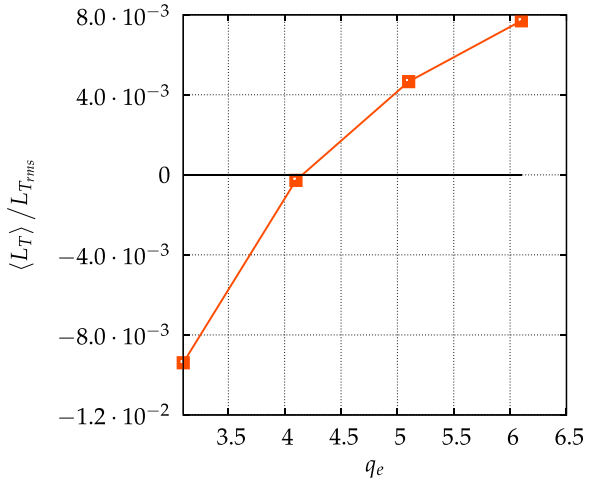


FIG. 31. Normalized toroidal angular momentum $\langle L_T \rangle / L_{T_{rms}}$ as a function of $q_e$.

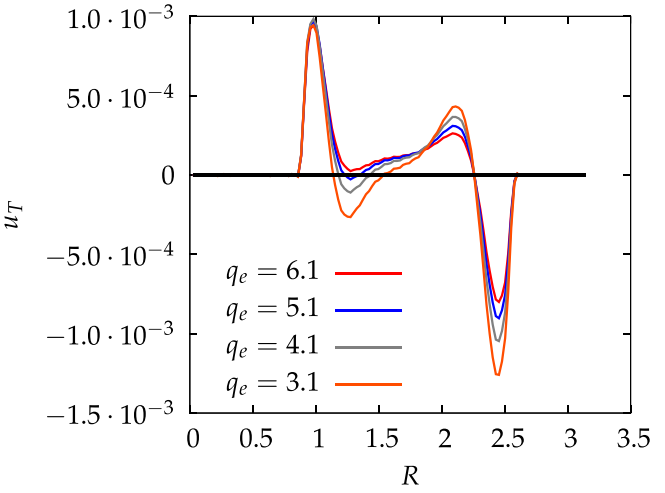


FIG. 33. Toroidal velocity profiles along a horizontal cut, at the center of the domain.

An important feature is the change of sign in the volume averaged toroidal angular momentum, found also in experimental observations,[30–32] when the toroidal magnetic field, hence the safety factor, is varied (Fig. 31). In our case, the averaged angular momentum changes completely in sign, it passes from negative to positive for increasing $q_e$. The two-dimensional azimuthally averaged toroidal velocities (Fig. 32) show the increase of the area in which the toroidal velocity is negative when the safety factor is decreased. For the lowest value of $q_e$ that we consider, the vertical cut (Fig. 32(d)) shows larger velocities and a small downward shift of the position where the toroidal velocity changes sign. This displacement enlarges the negative velocity area. The growth of the negative toroidal velocity is better visualized in the cuts along the direction of the big radius (Fig. 33). For decreasing $q_e$, the velocities tend to be more peaked and near the center of the torus a region appears where the toroidal velocity is negative. We notice that the change of sign of the toroidal velocity mainly occurs in the center of the geometry. Close to the boundaries the toroidal component grows but does not reverse sign.

As presented in Sec. III B small fluctuations around the azimuthal average exist. We see in Fig. 34 that the magnitude of these fluctuations is relatively insensitive to the value of the safety factor. The change is just of a few percent for the normalized velocity fluctuations. It is larger for the normalized magnetic fluctuations, but it remains below ∼20% (Fig. 35). Hence, the safety factor variation, in the considered range, does not increase substantially the non-axisymmetric perturbations.

### D. Influence of the reversal of the imposed toroidal magnetic field

The simulation with inverted toroidal magnetic field is performed for $q_e = 6.1$ and $M = 1131$. The results show that the velocity reverses sign in the whole domain (Fig. 36). The counterrotating poloidal vortices are unchanged, only the toroidal velocities are affected. In Fig. 36(c), the profiles are exactly symmetric with respect to the vertical axis. Basically, what happens is that the perturbed toroidal magnetic field reverses its sign and this generates an inverse poloidal current density. The existing poloidal magnetic field

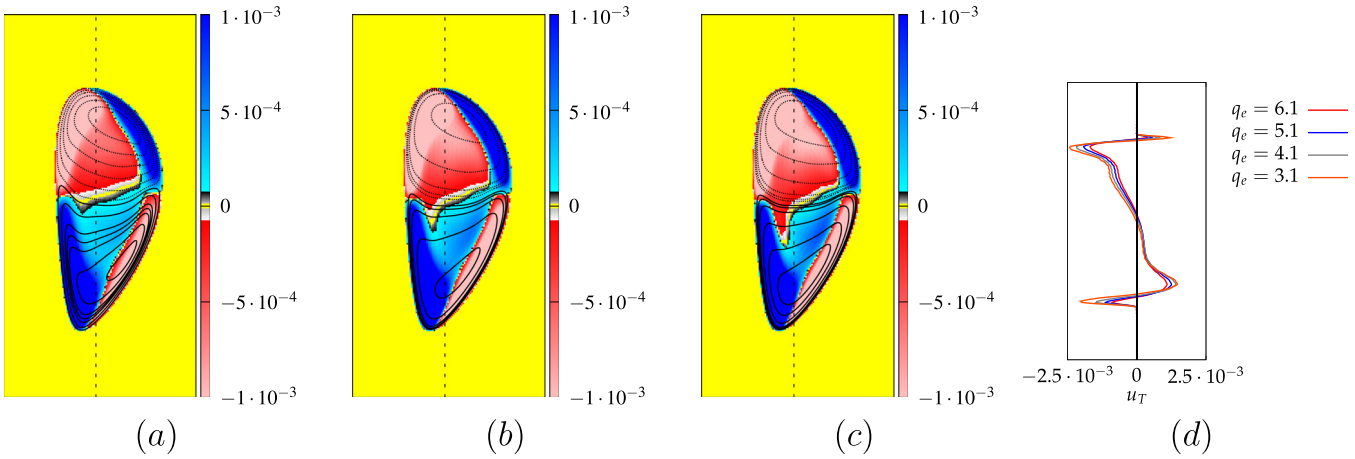


FIG. 32. Azimuthally averaged flow visualizations: toroidal velocity $u_T$ and poloidal stream function contours (solid line positive, dotted line negative contours) for $q_e = 6.1$ (a), $q_e = 4.1$ (b), and $q_e = 3.1$ (c). (d) Toroidal velocity profiles along a vertical cut. The position of these cuts is indicated in (a)–(c) by a dotted vertical line.

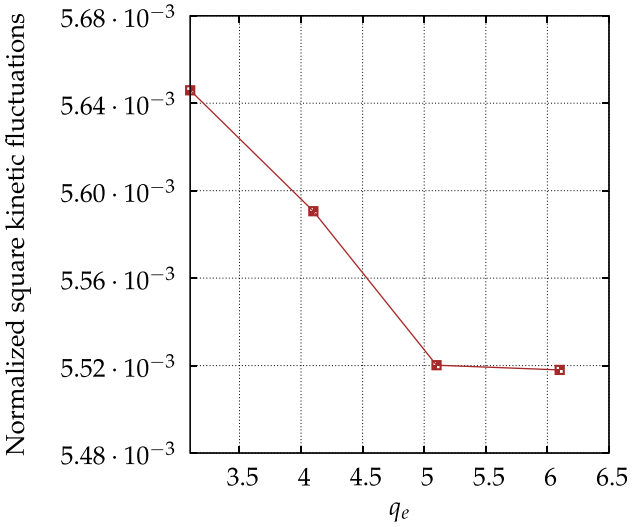


FIG. 34. Square velocity fluctuations normalized by the total square velocity.

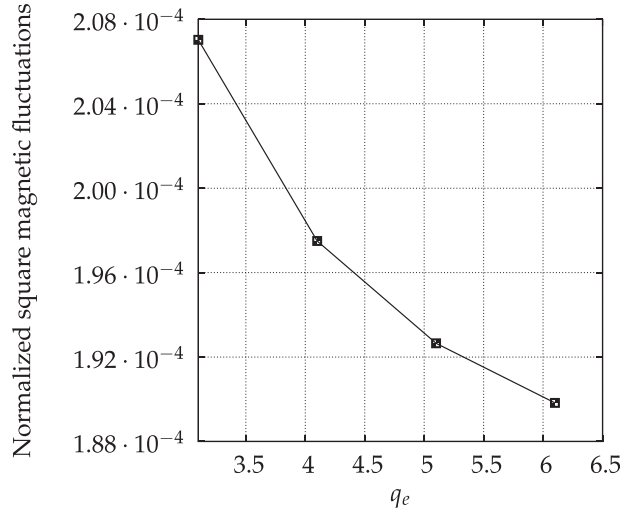


FIG. 35. Square magnetic fluctuations normalized by the total square perturbed magnetic field.

associated with the inverted poloidal current density field gives an opposite toroidal Lorentz force. Finally, this Lorentz force will make the toroidal velocities reverse in the whole domain. We can write the three components of the Lorentz force in cylindrical coordinates

$$\begin{cases} F_R = j_T B_Z - \dfrac{1}{R}\dfrac{\partial (RB_T)}{\partial R} B_T, \\ F_T = \dfrac{\partial B_T}{\partial Z} B_Z + \dfrac{1}{R}\dfrac{\partial (RB_T)}{\partial R} B_R, \\ F_Z = -\dfrac{\partial B_T}{\partial Z} B_T + j_T B_R. \end{cases} \tag{24}$$

The inversion of the sign of $B_T$ transforms the original Lorentz force vector $(F_R, F_T, F_Z)$ into $(F_R, -F_T, F_Z)$. Only the toroidal component is affected. Hence, the poloidal velocities are unchanged but the toroidal velocities are inverted.

## IV. CONCLUSION

In the present paper, it was demonstrated numerically, solving the fully nonlinear time-dependent viscoresistive MHD equations, that in a toroidal geometry, assuming constant transport coefficients, if the imposed toroidal magnetic and toroidal electric fields are irrotational, the conducting flow inside a torus necessarily moves. The reason for this is that the curl of the Lorentz force resulting of the imposed fields is nonzero. It follows that the gradient of a scalar (in this case the pressure) cannot balance the equation. Consequently, viscous dissipation is needed and vorticity is created.

For a low viscous Lundquist number, the system tends to produce small toroidal velocities, the dominant flow being a pair of counterrotating vortices in the poloidal plane. A change occurs when the viscous Lundquist number is increased. There is a transition from a dominantly poloidal to dominantly toroidal flow. This transition is in agreement

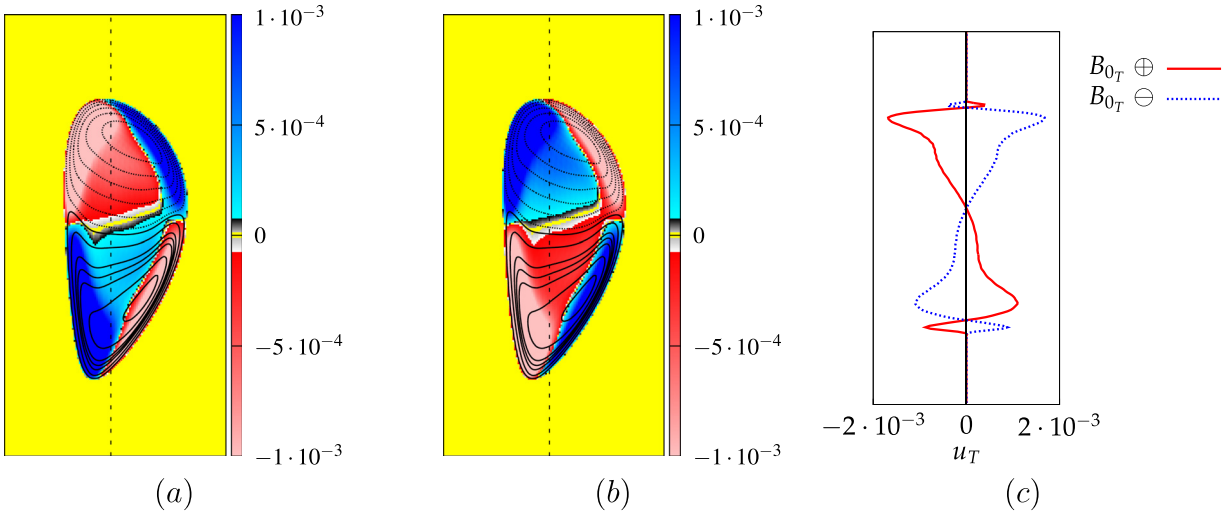


FIG. 36. Azimuthally averaged flow visualizations: toroidal velocity $u_T$ and poloidal stream function contours (solid line positive, dotted line negative contours) for imposed positive $B_{0_T}$ (a) and negative $B_{0_T}$ (b). (c) Toroidal velocity profiles along a vertical cut. The position of these cuts is indicated in (a) and (b) by a dotted vertical line.

with the tendency of the velocity field to align with the magnetic field.

Two different toroidal geometries are considered in the present study, one with an up-down symmetric and the other with an asymmetric cross section. A fundamental difference exists between both studied cases: the volume-averaged angular momentum is zero for the symmetric case, while for the asymmetric cross section a finite volume-averaged angular momentum appears. There is a breaking in the up-down symmetry of the flow and a toroidal preferred direction emerges.

Nevertheless, the kinetic energy decreases with increasing nonlinearity, since the total magnetic and current density fields tend to align in the center of the domain. The limitation in the numerical resources prevents the study of this system for larger viscous Lundquist numbers. It remains an open question if there will be a continuous increase of the alignment between the magnetic and current density field or if a transition exists.

When the safety factor is decreased while maintaining the transport coefficients constant, the kinetic and fluctuating magnetic energy become higher. The main qualitative effect is the influence on the toroidal velocity direction. There is a change in the volume-averaged angular momentum that reverses sign. For low $q_e$, it is negative and at large safety factors it becomes positive. Near the boundaries, the toroidal velocity direction remains unchanged.

The last part of the study was dedicated to the influence of the reversal of the toroidal magnetic field. It is shown that it plays a role only in the toroidal velocities. The reversal changes the sign of the poloidal current density, which gives rise to the toroidal Lorentz force. In consequence, the toroidal force reverses in the whole volume making the toroidal velocities reverse their direction compared to the original case. The poloidal velocities are unchanged.

We conclude this work by stressing that this mechanism stands in contrast to the Grad-Shafranov equilibrium between the pressure gradient and the Lorentz-force, Eq. (8). The Grad-Shafranov equilibrium holds approximately, but the small imbalance leads to the dynamics that we have reported in the present paper.

## ACKNOWLEDGMENTS

We acknowledge financial support from the French Research Agency (ANR), project SiCoMHD, contract ANR-11-BLAN-045, as well as IDRIS for computing time (project number 22206). We further acknowledge discussion with Professor Caroline Nore.

## APPENDIX: CALCULATION OF THE IMPOSED POLOIDAL MAGNETIC FIELD

We construct the magnetic field satisfying the following properties: (i) it corresponds to a current density profile $\propto 1/R$, (ii) it is parallel to the wall, and (iii) it is solenoidal. With respect to our previous investigation[33] the magnetic topology is changed. In fact in the previous paper, the imposed poloidal magnetic field satisfied the imposed toroidal current density profile $\boldsymbol{j}_{0_T}$ and the solenoidal constraint but the normal component did not vanish (as is shown in Fig. 37(c)). To solve this problem and to satisfy the three desired conditions, we obtain $\boldsymbol{B}_{0_{pol}}$ from the current density by writing in terms of a vector potential $\boldsymbol{B}_{0_{pol}} = \nabla \times \boldsymbol{A}_0|_{pol}$, where $\boldsymbol{A}_0 = A_{0_T}\boldsymbol{e}_T$.

The poloidal magnetic field is calculated from the imposed toroidal current density distribution $\boldsymbol{j}_{0_T}$. It can be obtained using the vector potential, $\boldsymbol{B}_{0_{pol}} = \nabla \times \boldsymbol{A}_0|_{pol}$, where $\boldsymbol{A}_0 = A_{0_T}\boldsymbol{e}_T$. Using the Coulomb Gauge, we have the following Poisson equation[34]

$$\nabla^2(A_{0_T}\boldsymbol{e}_T) = -\boldsymbol{j}_{0_T}. \tag{A1}$$

The associated boundary condition is the normal component of the magnetic field vanishing at the boundary of the torus.

It is equivalent and more convenient to work with the magnetic flux function $\chi(R,Z) = RA_{0_T}$, directly. The axisymmetric poloidal magnetic field is easily derived from the flux function $\chi(R,Z)$

$$\boldsymbol{B}_{0_{pol}} = \nabla\chi \times \nabla T, \tag{A2}$$

with $\nabla T = (1/R)\boldsymbol{e}_T$. Substituting this into Ampère's law, $\nabla \times \boldsymbol{B}_{0_{pol}} = j_{0_T}\boldsymbol{e}_T$ yields

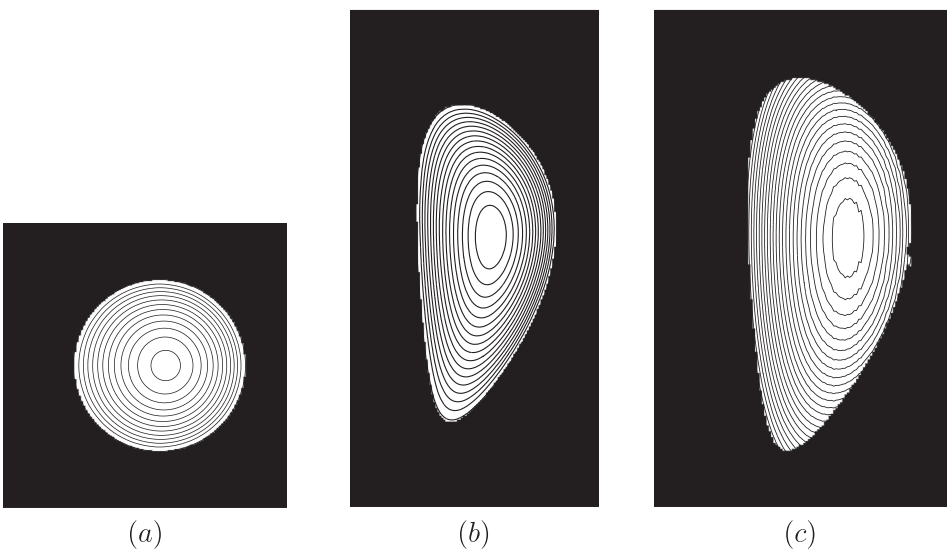


FIG. 37. Poloidal magnetic field lines ($\chi = RA_{0_T}$ = constant) for the different cross sections: (a) symmetric and (b) asymmetric. In (c), we show the field lines for the asymmetric geometry used in Ref. 33.

$$\Delta^* \chi = \frac{\partial}{\partial R}\left(\frac{1}{R}\frac{\partial \chi}{\partial R}\right) + \frac{1}{R}\frac{\partial^2 \chi}{\partial Z^2} = -j_{0_T}. \tag{A3}$$

The boundary condition $\boldsymbol{B}_{0_{pol}} \cdot \boldsymbol{n}|_{wall} = 0$ implies a Dirichlet boundary condition on the magnetic flux function $\chi|_{wall} = \text{constant}$.

Numerically the calculation of the poloidal magnetic field $\boldsymbol{B}_{0_{pol}}$ is performed solving the previous Poisson equation for the magnetic flux function $\chi$. This equation is solved with a Fourier spectral method and the volume-penalization technique is used to impose the Dirichlet boundary condition at the wall.[3] The resulting computed equation is the following:

$$\frac{\partial \chi}{\partial t} = \lambda \Delta^* \chi + \lambda j_{0_T} - \underbrace{\frac{\Xi(\boldsymbol{x})}{\eta}(\chi - \chi_{wall})}_{\textit{Penalisation term}}. \tag{A4}$$

Here, $\lambda$ is a diffusion coefficient ($\lambda = 1$), $\Xi$ is the mask function (it takes the value zero in the region where the Poisson equation needs to be solved and one in the rest of the computational domain), and $\eta$ is the penalization parameter ($\eta = 5 \times 10^{-4}$). The size of the domain is $(2\pi)^3$ for the asymmetric and $(2\pi \times 2\pi \times \pi)$ for the symmetric cross section with a resolution of $256^3$. The value of the Dirichlet boundary condition is $\chi_{wall}$. This equation is evolved in time, reaching a steady state, numerically $\| \chi^{n+1} - \chi^n \| < 10^{-6}$. We then recover with sufficient accuracy the solution of the Poisson equation (A3) taking into account the Dirichlet boundary condition via the penalization term. The solution of this pre-computation will give our basis magnetic field $\boldsymbol{B}_0$ which will be kept constant during the actual simulation.

The resulting poloidal magnetic topology is presented in Figs. 37(a) and 37(b), respectively, for the considered symmetric and asymmetric geometries (Fig. 1).


[1]L. Kamp and D. Montgomery, Phys. Plasmas **10**, 157 (2003).
[2]L. Kamp and D. Montgomery, J. Plasma Phys. **70**, 113 (2004).
[3]J. Morales, M. Leroy, W. Bos, and K. Schneider, J. Comput. Phys. **274**, 64 (2014).
[4]J. Rice, A. Ince-Cushman, L.-G. Eriksson, Y. Sakamoto, A. Scarabosio, A. Bortolon, K. Burrell, B. Duval, C. Fenzi-Bonizec, M. Greenwald *et al.*, Nucl. Fusion **47**, 1618 (2007).
[5]D. Pfirsch and A. Schlüter, *Der Einfluss der elektrischen Leitfähigkeit auf das Gleichgewichtsverhalten von Plasmen niedrigen Drucks in Stelleratoren*, Technical Report MPI/PA/7/62 (Max-Planck-Institute, Munich, 1962).
[6]X. Garbet, Y. Idomura, L. Villard, and T. Watanabe, Nucl. Fusion **50**, 043002 (2010).
[7]A. Aydemir, Phys. Rev. Lett. **98**, 225002 (2007).
[8]A. Aydemir, Phys. Plasmas **14**, 056118 (2007).
[9]S. Pamela, G. Huysmans, and S. Benkadda, Plasma Phys. Controlled Fusion **52**, 075006 (2010).
[10]P. Angot, C.-H. Bruneau, and P. Fabrie, Numerische Mathematik **81**, 497 (1999).
[11]S. Neffaa, W. Bos, and K. Schneider, Phys. Plasmas **15**, 092304 (2008).
[12]K. Schneider, Comput. Fluids **34**, 1223 (2005).
[13]W. Bos, S. Neffaa, and K. Schneider, Phys. Rev. Lett. **101**, 235003 (2008).
[14]J. Berkowitz, H. Grad, and H. Rubin, "Magnetohydrodynamic stability," in United Nations International Conference on the Peaceful Uses of Atomic Energy (1958), p. 177.
[15]V. Shafranov, Rev. Plasma Phys. **2**, 103 (1966).
[16]J. Bates and D. Montgomery, Phys. Plasmas **5**, 2649 (1998).
[17]J. Manickam, Nucl. Fusion **24**, 595 (1984).
[18]S. Cappello and D. Escande, Phys. Rev. Lett. **85**, 3838 (2000).
[19]X. Shan and D. Montgomery, Plasma Phys. Controlled Fusion **35**, 619 (1993).
[20]D. Montgomery and X. Shan, Comments Plasma Phys. Controlled Fusion **15**, 315 (1994).
[21]J. Bates and R. Lewis, Phys. Plasmas **3**, 2395 (1996).
[22]J. Wesson, *Tokamaks* (Oxford University Press, 2004).
[23]D. Montgomery, J. Bates, and R. Lewis, Phys. Plasmas **4**, 1080 (1997).
[24]L. Zakharov and V. Shafranov, Rev. Plasma Phys. **11**, 153 (1986).
[25]L. Kamp, D. Montgomery, and J. Bates, Phys. Fluids **10**, 1757 (1998).
[26]Y. Camenen, A. Peeters, C. Angioni, F. Casson, W. Hornsby, A. Snodin, and D. Strintzi, Phys. Rev. Lett. **102**, 125001 (2009).
[27]Y. Camenen, A. Bortolon, B. Duval, L. Federspiel, A. Peeters, F. Casson, W. Hornsby, A. Karpushov, F. Piras, O. Sauter *et al.*, Plasma Phys. and Controlled Fusion **52**, 124037 (2010).
[28]JET-Team, Nucl. Fusion **32**, 187 (1992).
[29]J. Dahlburg, D. Montgomery, G. Doolen, and L. Turner, J. Plasma Phys. **40**, 39 (1988).
[30]J. Rice, B. Duval, M. Reinke, Y. Podpaly, A. Bortolon, R. Churchill, I. Cziegler, P. Diamond, A. Dominguez, P. Ennever *et al.*, Nucl. Fusion **51**, 083005 (2011).
[31]J. Rice, M. Greenwald, Y. Podpaly, M. Reinke, P. Diamond, J. Hughes, N. Howard, Y. Ma, I. Cziegler, B. Duval *et al.*, Phys. Plasmas **19**, 056106 (2012).
[32]A. Scarabosio, A. Bortolon, B. Duval, A. Karpushov, and A. Pochelon, Plasma Phys. Controlled Fusion **48**, 663 (2006).
[33]J. Morales, W. Bos, K. Schneider, and D. Montgomery, Phys. Rev. Lett. **109**, 175002 (2012).
[34]D. Montgomery, J. Bates, and S. Li, Phys Fluids **9**(4), 1188 (1997).